Numerical Parametric Study of Hydrodynamic Ram

Y Kwon[1]*, K Yun[2]

1. Department of Mechanical and Aerospace Engineering, Naval Postgraduate School, CA, USA

2. Agency for Defense Development, Yuseong, South Korea

ABSTRACT

A numerical parametric study was conducted to better understand the Hydrodynamic Ram (HRAM) event. The model considered a projectile penetrating a box which contains water either partially or fully. A standard model was developed and validated against the available experimental data. Then, each parameter was varied individually to determine its effect during the HRAM event. The parameters considered were the water filling level in the box, its wall thickness, projectile impact velocity, projectile mass, impact angle, and projectile shape. The effect of each individual parameter was studied, and the effects of different parameters were compared. Then, an attempt was made to predict the combined effects of multi-variables. Even though the results and discussion are for the specific geometric and material data used in this study, the present findings are expected to provide valuable insights to the qualitative characteristics of the HRAM event.

1. INTRODUCTION

Hydrodynamic Ram (HRAM) is a phenomenon which occurs as a high velocity projectile penetrates a tank or vessel containing fluids and transfers its momentum and kinetic energy to the surrounding fluids whose shock pressure also damages the container. The HRAM damage may occur in various fluid storage tanks including fuel tanks. An aircraft operating at low altitude may be hit by a small projectile fired at it. This results in HRAM when the projectile penetrates the fuel tank.

The HRAM consists of four different phases, and they are called shock phase, drag phase, cavitation phase, and exit phase. Depending on each case, all those phases may not occur. For example, if the projectile does not have enough kinetic energy to penetrate a structure, the projectile may neither enter the structure not exit the structure.

The study of HRAM event was conducted intensively during 1970's [1-9]. There were experimental measurements and simplified predictions. More recently, more emphasis has been placed on the development of numerical techniques to simulate this complex fluid structure interaction problem. The Arbitrary Lagrangian-Eulerian (ALE) technique is a finite element formulation in which the computational domain is a prior neither fixed in space such as the Eulerian-based formulation nor attached to materials such as the Lagrangian-based formulation. The ALE-based simulations can alleviate many of the

*Corresponding Author: ywkwon@nps.edu

drawbacks that the traditional Lagrangian-based and Eulerian-based finite element simulations have. The ALE-based formulation can be reduced to either the Lagrangian-based formulation by equating the mesh motion to material motions or the Eulerian-based formulation by fixing the mesh in space. Therefore, an ALE code is suitable to perform engineering simulations such as fluid-structure interactions problems such as HRAM.

The early research on HRAM using the finite element technique was undertaken in 1980 [10]. The mesh had a large distortion because the computer analysis used the Lagrangian finite element formulation. As a result, this affected the accuracy of the numerical solution. Later, the coupling techniques of Eulerian and Lagrangian formulations were developed and applied to the HRAM problems. Recently, the smoothed particle hydrodynamics technique was developed for modeling the fluid domain and applied to HRAM [11–15]. Those papers investigated numerical techniques to validate and verify their solutions for the HRAM event. To the authors' best knowledge, there was no extensive parametric study so as to better understand the effect of each different parameter on the HRAM event as well as to predict their effects. This information is very useful for designing any fluid container against the HRAM effect. As a result, a series of parametric studies were conducted for the HRAM event numerically using the LS-Dyna code [16].

The subsequent section describes the base numerical model used in the study and its validation against available experimental data. Then, numerical results and discussion from a parametric study are provided by varying each parameter in the base model one by one. The main focus was placed to understand the effect of each parameter, to compare the effects of different parameters, and to develop predictive equations for change in those parameters. Even though the developed equations may be only suitable for the given geometric and material data used in the present study, they are expected to provide at least qualitative characteristics of each parameter's effect. Finally, conclusions and the summary of the major findings are provided at the end.

2. NUMERICAL MODELING

The numerical models were developed using the commercial finite-element code called LS-Dyna v.971 [16]. In order to study the HRAM phenomenon, the ALE method was adopted to model a fluid inside a structure. This section describes the computer model in detail. The model represents the nominal or base case from which a parametric study was conducted. When a parametric study is presented, the selected variable is discussed regarding how it is varied from the nominal value.

2.1. Box and projectile finite element model

A box structure was used for the present study. The symmetry of the structure under consideration allows modeling only a quarter of the whole box as shown in Fig. 1. Since the nature of this simulation demands a very high density mesh, such a reduction in the model size is very desirable. The box is divided into three parts, the walls impacted by the projectile (entry and exit walls), the lateral wall and the PMMA window as studied in Ref. [12]. The geometric dimension of the box and its wall thickness are provided in Fig. 1(a).

The impacted walls and the PMMA window were discretized by means of eight-node solid elements with reduced integration. A refined mesh was used around the impact zone, and a progressively coarser mesh was used as the distance to the striking point became larger. The

impacted walls had five elements through the thickness, and the elements in the impact zone were 1 mm in the other two directions. Based on the mesh sensitivity study, the mesh size was considered appropriate to reproduce the behavior of the solids in the impacted zone. Four-node shell elements were chosen to discretize the other wall in order to reduce the number of elements. Finally, the mesh of the box consisted of 25,300 elements as shown in Table 1. The material properties and parameters used for this model are provided in Table 2. The Johnson–Cook strain hardening constitutive equation [17] was selected to model the aluminum of the box as the projectile impacts and penetrates the aluminum surface. The Johnson-Cook plasticity model is expressed as

$$\sigma_y = \left[A + B\left(\varepsilon^p\right)^n \right]\left(1 + C\ \ln\dot{\varepsilon}\right)\left[1 - \left(T^*\right)^m\right] \tag{1}$$

where σ_y, ε^p, and $\dot{\varepsilon}$, and T^* are the yield stress, effective plastic strain, strain rate, and the temperature ratio like

$$T^* = \frac{T - T_{room}}{T_{melt} - T_{room}}$$

Here, subscripts 'room' and 'melt' indicate the room and melting temperatures, respectively. The rest of coefficients for Eq. (1) are provided in Table 2. The effective plastic strain at failure was selected to be 0.2.

The projectile is a solid sphere with its diameter 12.5 mm and mass 8g. It is made of steel as listed in Table 2, and the initial impact velocity is 900 m/s. It is divided into 1000 eight node solid elements. The projectile strikes the center of the entry wall at the perpendicular direction.

Table 1. Material and Element for Solid

Part Name	**Type**	**Material Name**	**Element number**
Impact wall (entry & Exit)	Solid	6063-T5	19,750
Other wall	Shell		1,800
PMMA window	Solid	PMMA	3,750
Projectile	Solid	Rigid	1,000

Table 2. Material Properties for the solids

Material	**ρ (kg/m^3)**	**E (GPa)**	**υ**	**A (GPa)**	**B (GPa)**	**n**	**C**	**m**
6063-T5 Aluminum	2700	71	0.33	0.2	0.144	0.62	0	1
Steel	7830	207	0.28	-	-	-	-	-
PMMA	1180	3	0.35	-	-	-	-	-

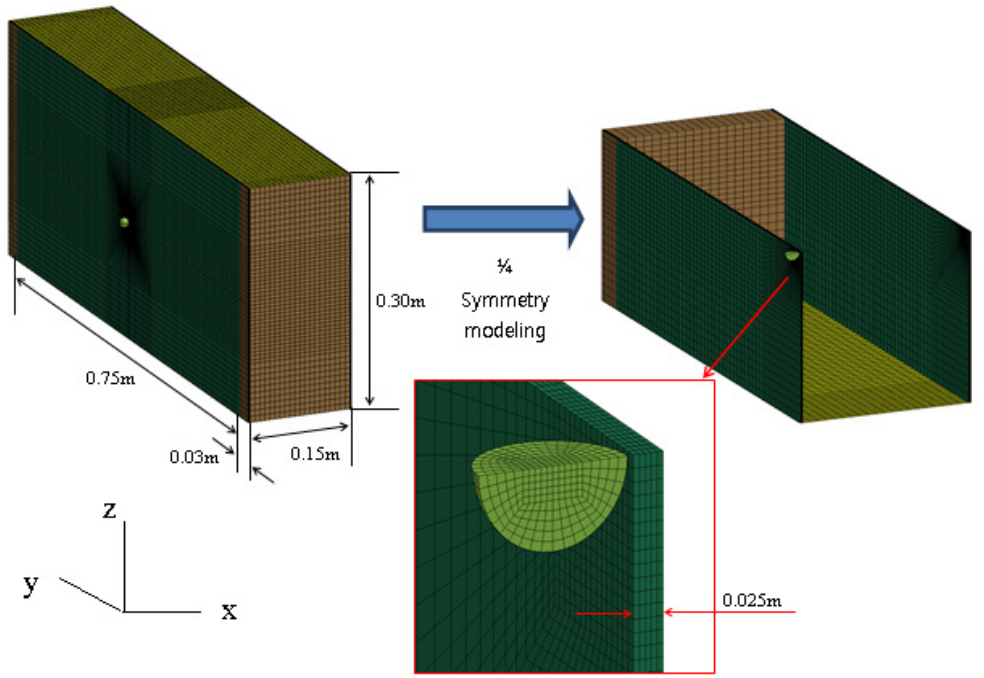

(a) Box and projectile finite element models

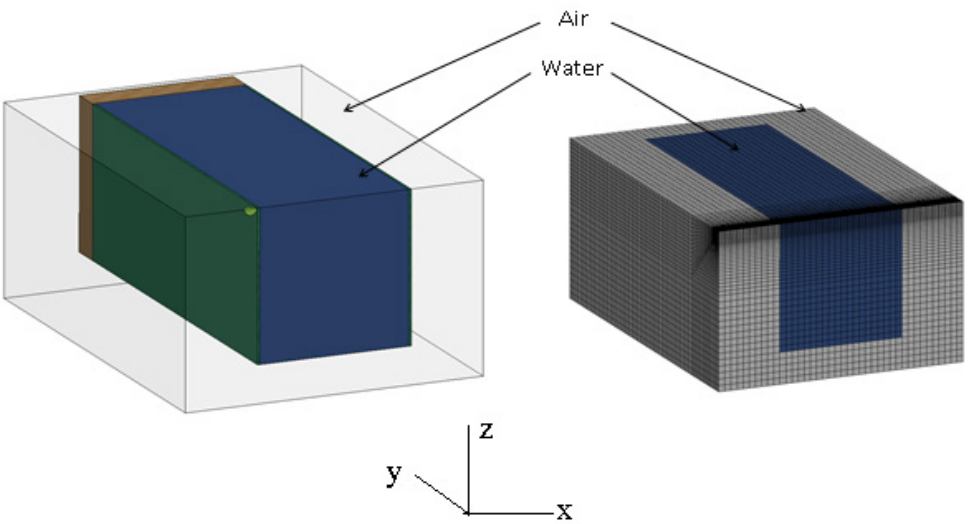

(b) Fluid models

Figure 1. Finite element models using the ALE approach.

2.2. Fluid finite element model

It is expected that the fluid inside the box undergoes large motions such that the Eulerian description is selected for fluid. As a result, a multi-material ALE formulation was chosen for the treatment of the fluid. Multi-material means that each element of the mesh has the ability to contain two or more materials, in this case water and air.

The fluid inside the box is discretized by means of eight-node solid elements. Strictly, the fluid is discretized by means of an Eulerian mesh as shown in Fig 1(b). Modeling the air region is essential to allow the water to flow inside the box. This is only possible if the water and air meshes share the same nodes at their interface. The fluid inside the box and the surrounding air region has 96,000 elements, as listed in Table. 3. The properties and parameters used in the simulation for the water and the air are given in Table 4.

Water was modeled using the Gruneisen equation of state as given below:

$$p=\frac{\rho_o C^2\mu\left[1+\left(1-\frac{\gamma_o}{2}\right)\mu-\frac{a}{2}\mu^2\right]}{\left[1-(S_1-1)\mu-S_2\frac{\mu^2}{\mu+1}-S_3\frac{\mu^3}{(\mu+1)^2}\right]^2}+(\gamma_o+a\mu)\Phi \tag{2}$$

where p, and Φ are the pressure and internal energy per initial volume; and $\mu=\frac{1}{V}-1$. Here V is the relative volume. The parameters ρ_o and γ_o are the density and Gruneisen gamma, and a is the parameter of the volume correction to γ_o as the first order. All other material coefficients are provided in Table 4. The air was modeled using the linear polynomial equation of state as below:

$$p=(C_4+C_5\mu)E \tag{3}$$

in which the coefficients are also listed in Table 4.

Table 3. Material and Element for Fluid

Part Name	**Element Type**	**Element Number**
Water	Solid	39,500
Air	Solid	56,500

Table 4. Material Properties for the Fluid

Material	ρ_o**(kg/m^3)**	ν**(m/s^2)**	**C(m/s)**	**S_1**	**S_2**	**S_3**	**γ_0**	**a**	**C_4**	**C_5**	**E_0(J/m^3)**
Water	1000	$0.89*10^{-3}$	1448	1979	0	0	0.11	3	-	-	-
Air	1.22	$1.77*10^{-5}$	-	-	-	-	-	-	0.4	0.4	$2.53*10^5$

2.3 Model validation

In order to validate the computer model before the parametric study, the numerical results were compared to the experimental data [12]. The test was conducted for a square cross-sectional aluminum tube which was 2.5 mm thick, 150 mm wide and 750 mm long. The tube was impacted by a steel sphere with the speed 900 m/s, mass 8g and diameter 12.5 mm. The numerical model is the same as the nominal model described above. The same data were used in the numerical model. The projectile displacement was compared between the two results as shown in Fig. 2. They agree very well. More refined meshes would improve the numerical results. However, based on the balance between the accuracy and computational time, the present mesh was decided to be used without any further refinement.

Applying Newton's 2nd law to a projectile with drag force yields

$$-m_p \frac{d\mathrm{v}}{dt} = \frac{1}{2} C_D A_P \rho_f v^2 \tag{4}$$

where v is the projectile velocity, m_p is the projectile mass, C_D is the drag coefficient, A_p is the cross-sectional area of the projectile, and ρ_f is the fluid density. Assuming the drag coefficient is constant, Eq. (4) gives the following expression for a spherical projectile velocity

$$\frac{v}{v_o} = \frac{1}{1 + \frac{3}{4} C_D \left(\frac{\rho_f v_o}{\rho_p d_p} \right) t} \tag{5}$$

in which v_o is the initial velocity, t is time, ρ_p is the projectile mass density, and d_p is the projectile diameter. One more integration results in the projectile travelling distance as below

$$x = \frac{1}{\frac{3}{4} C_D \left(\frac{\rho_f}{\rho_p d_p} \right)} \ln \left[\frac{3}{4} C_D \left(\frac{\rho_f v_o}{\rho_p d_p} \right) t + 1 \right] \tag{6}$$

where x is the travelling distance of the projectile. The results predicted using Eq. (6) is also plotted in Fig. 3, and the predicted travel distance agrees well with the experimental data. This suggests that a representative drag coefficient may be assumed constant throughout the projectile motion with reasonable accuracy.

The cavity sizes behind the projectile are compared between the experimental and numerical data at three different times in Fig. 3. They compare very well. In addition, the pressure in the fluid is also compared between the two results at two locations as shown in Fig. 4. The initial peak pressure agrees very well between the experimental and numerical solutions. There were some pressure oscillations in the numerical results following the initial peak pressures as compared to the experimental data. However, the oscillatory magnitudes are

much smaller than the initial peak value. The difference is believed to be resulting from damping. The experimental set-up has more damping than the numerical model because the latter does not include explicit damping in the model. Finally, energy was plotted in Fig. 5 to check the conservation of the total energy.

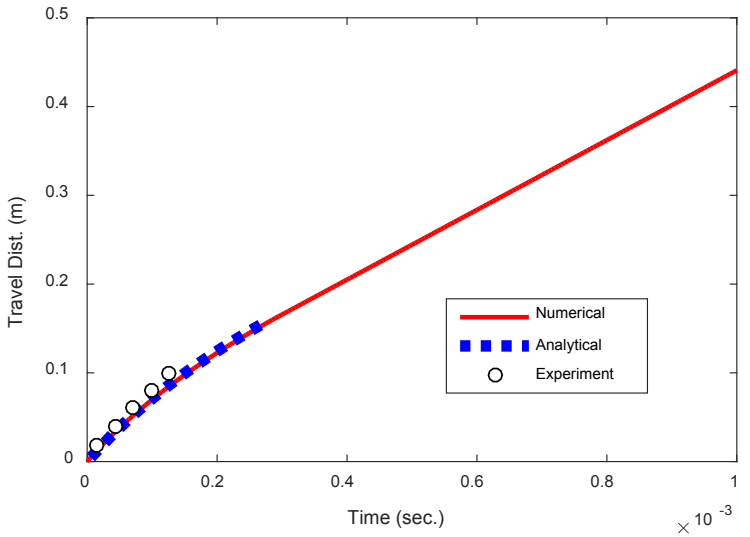

Figure 2. Comparison of projectile positions between the numerical and experimental results.

3. NUMERICAL RESULTS AND DISCUSSION

Several different parameters were considered in the study. One parameter was varied at a time based on the nominal model as described in the last section. The parameters were the water filling level, wall thickness of structure, projectile impact velocity, projectile mass, impact angle, and projectile shape. In the following subsections, each parameter was discussed individually in the order as stated above.

3.1. Water filling level

The water filling level was changed in the box. They were 0%, 25%, 40%, 50%, 60%, 75%, and 100%. Figure 6 shows the projectile motion along the z-axis inside the box with different water levels. If the water level is less than 50%, the projectile does not interact with the water because the projectile penetrates through the center of the box. Therefore, the figure only incudes the water level with at least 50%. The z-axis is along the height of the box. The lower part of the z-axis has water and the upper part has air for a partially filled box. When the water level is 50%, the air-water interface inside the box is at the level at which the projectile stoke the entry face. As a result, when the water level is less than 50%, the projectile does not get wet during its travel inside the box. When the water level is 50%, the projectile is wet partially in the beginning. Then, the pressure differential between the wet and dry surfaces of the projectile quickly pushed the projectile toward the air side (i.e.,

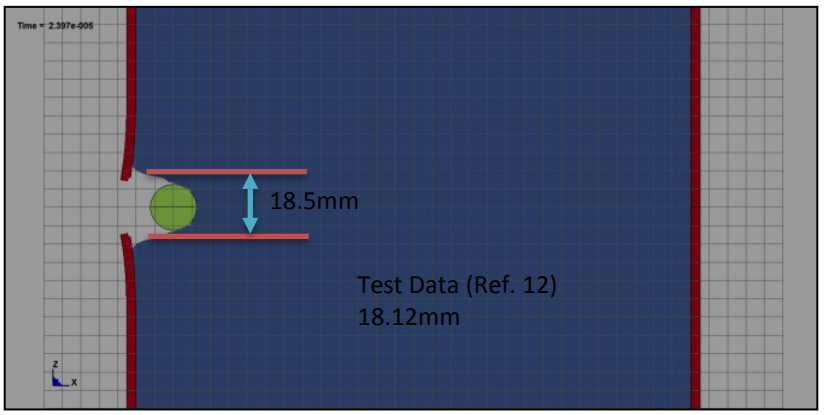

(a) At time 0.024 msec.

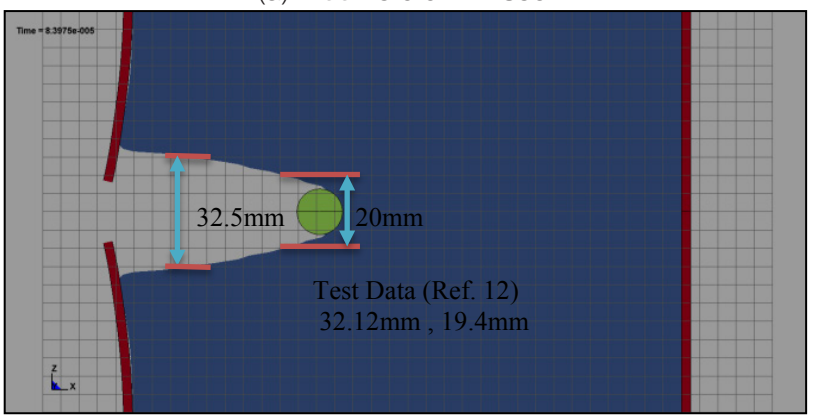

(b) At time 0.084 msec.

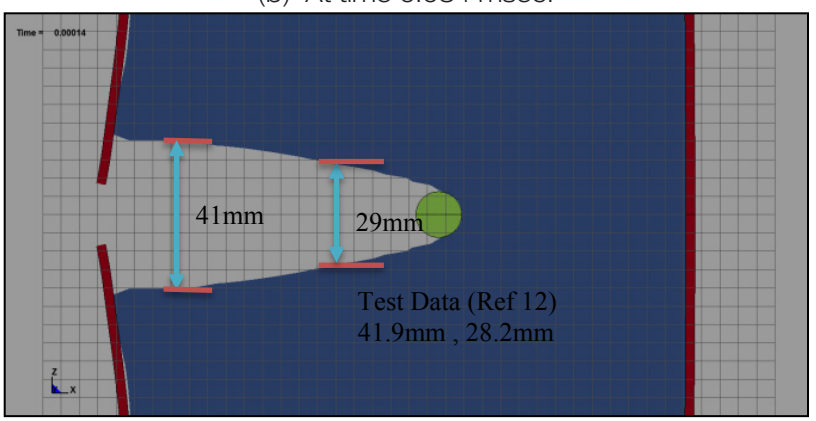

(c) At time 0.140 msec.

Figure 3. Comparison of experimental and numerical results for cavity sizes behind the projectile for three different times

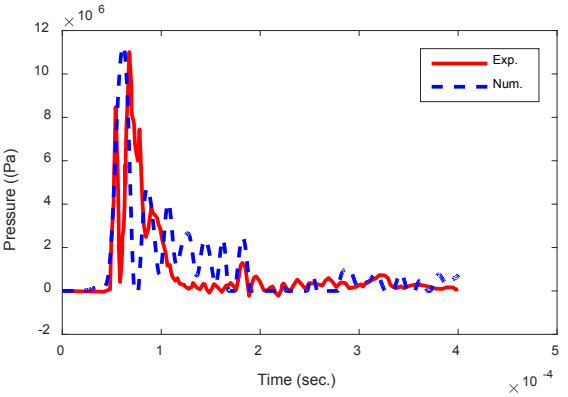

(a) Pressure at sensor 1

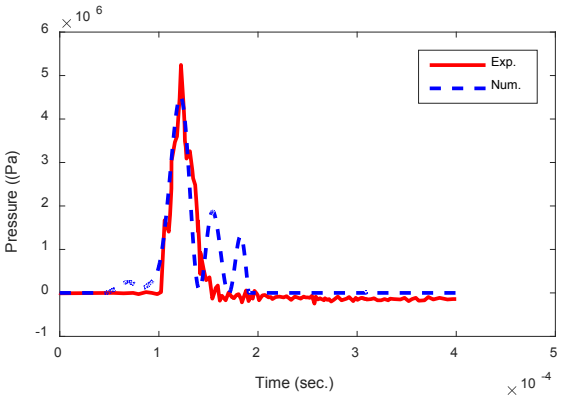

(b) Pressure at sensor 2

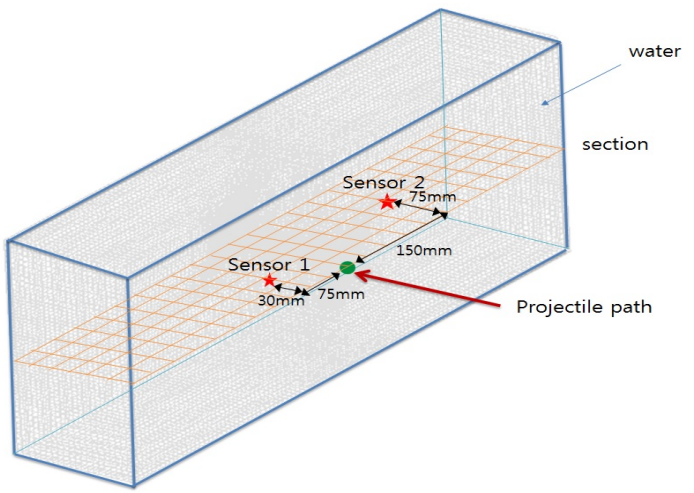

(c) Sensor location

Figure 4. Comparisons of pressures between the numerical and experimental studies and the sensor location.

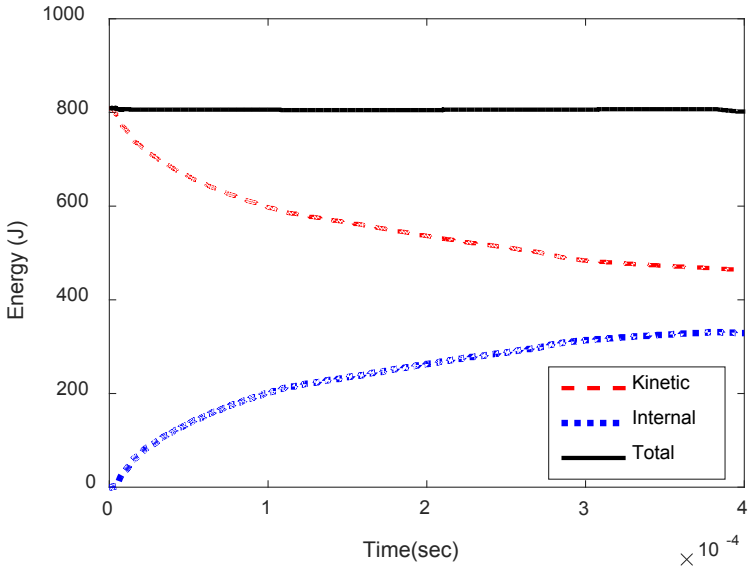

Figure 5. Plot of energy variation as a function of time

the positive z-direction in Fig. 6). When the water level is much greater than 50%, the projectile is in the water throughout the travel inside the box. However, there were deviations in the path of travel from the center line (z=0 in Fig. 6) except for the 100% full case. The projectile moved downward initially and then moved upward as shown in the figure. The deviation was greater for the 60% full box than the 75% full box.

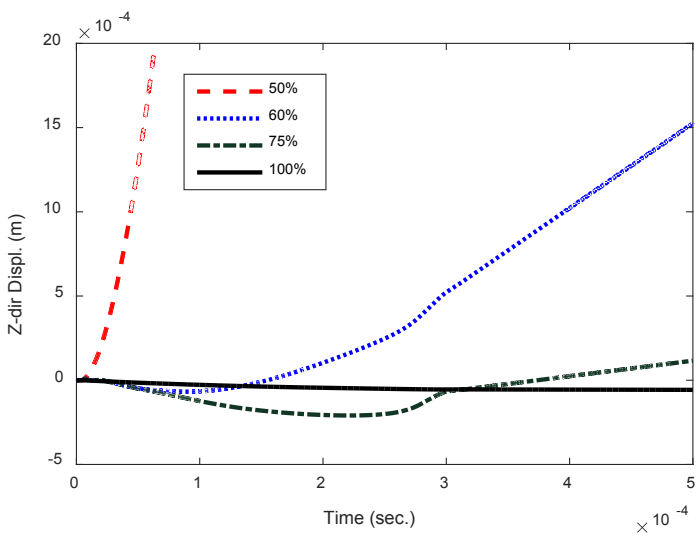

Figure 6. Plot of projectile displacement along the z-axis in the box for different water filling levels

When the projectile does not contact with water, the travel distance varies linearly with time as expected. When the water filling level is 50% and greater, the drag in the water reduces the speed of the projectile resulting in less travel distance for the given time. Because of the deviation from the horizontal path, it took a little longer time for the projectile to travel through the 60% or 75% full box than the 100% full box in order to arrive at the exit wall. For the 50% full box, partial wetting in the beginning applied the asymmetric drag and pressure to the projectile so that the projectile was pushed out of water resulting in a constant velocity without drag at later times as shown in Fig. 6 which compares the velocities for different water filling levels.

Examining the projectile velocity at the exit wall, there is a steep drop in the velocity for the 50% full box as shown in Fig. 7. However, there is no sizable drop in the projectile velocity for the exit wall with the 60% or more water full box. That is because the high water pressure already results in damage in the exit wall before the projectile reaches it. Therefore, the projectile can easily pass through the exit wall without much loss in its speed.

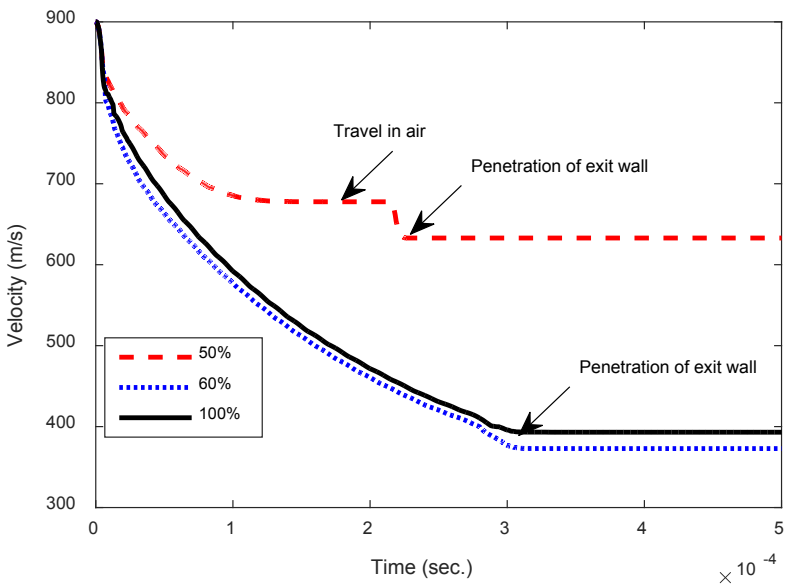

Figure 7. Comparison of velocities for different water filling levels

Figure 8 compares the cavity shape inside the box at time 1 msec. for different water levels. Because the projectile moved out of water for the 50% full case, the cavitation did not reach the exit wall. The figure also shows different deformations of the entry and exit walls depending on the water level. The detailed deformation plots are provided in Fig. 9. The higher water level resulted in greater deformations of both entry and exit walls. The gap between the last data points and the right-side vertical line in Fig. 9 indicates the hole radius induced by the projectile. The hole size was almost identical for all cases. However, the higher water level resulted in a larger gradient of deformation of the hole. This suggests that the shock pressure in water is greater with a higher water level.

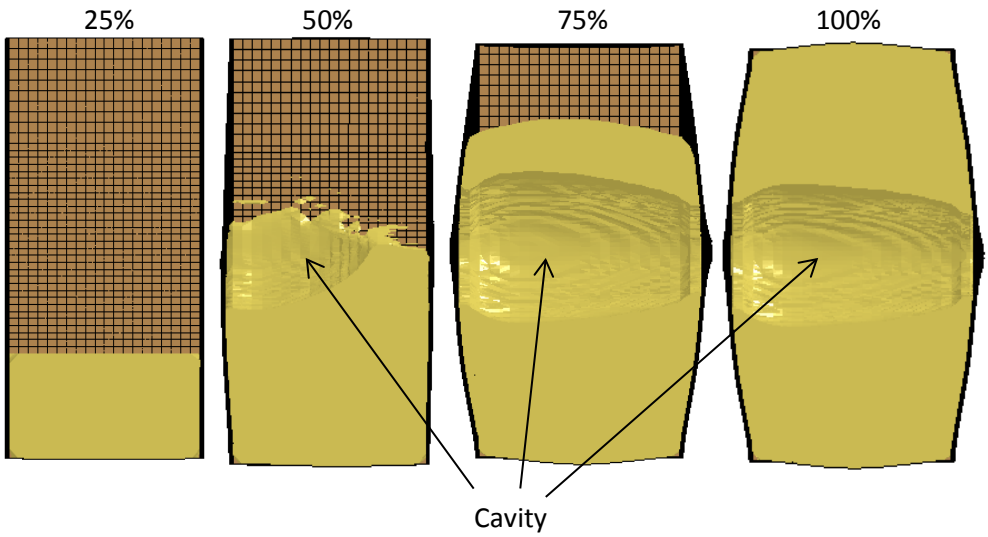

Figure 8. Comparison of cavity shapes for different water levels at time 1 msec.

Figure 10 shows the comparison of residual plastic strains in the entry wall for different water levels; 25%, 50%, 75% and 100%. In this study, material failure was determined based on the erosion criterion with the critical value of the equivalent plastic strain equal to 0.2. The higher water level resulted in greater plastic strains in the entry wall. While the 50% water level yielded larger plastic strain at the bottom side, all other water levels showed almost the same plastic strains at the top and bottom sides. Comparing plastic strains between the entry and exit walls for the same water level, the exit wall had greater plastic strains than the entry wall consistently. This suggests that even though the impact velocity is much greater on the entry wall than the exit wall, the fluid shock pressure produces greater plastic strains in the exit wall.

Figure 11 shows that fluid pressure at a location inside the box increases as the water level increases from the full case. Such a drop is quite notable. The peak pressure and the water filling level can be well represented using the equation

$$p_{\max} = -2\text{x}10^7 (h-0.5)^2 + 2\text{x}10^7 (h-0.5) + 5\text{x}10^5 \tag{7}$$

where h is the water level in fraction so that $h=1$ for the completely full box. The equation is valid $h \geq 0.6$ for the fitted data, and it shows that the increment in the peak pressure $\Delta p_{\max}$ becomes smaller as the water level h increases. Figure 4(c) shows the location of pressure measurement.

Figure 12 shows contours of the fluid shock waves across the box for three different water levels; 50%, 75%, and 100%. The most left figure is when the projectile is at the first quarter length of the box, the center figure is when the projectile at the center of the box, and the most right figure is when the projectile is at the last quarter length of the box. While

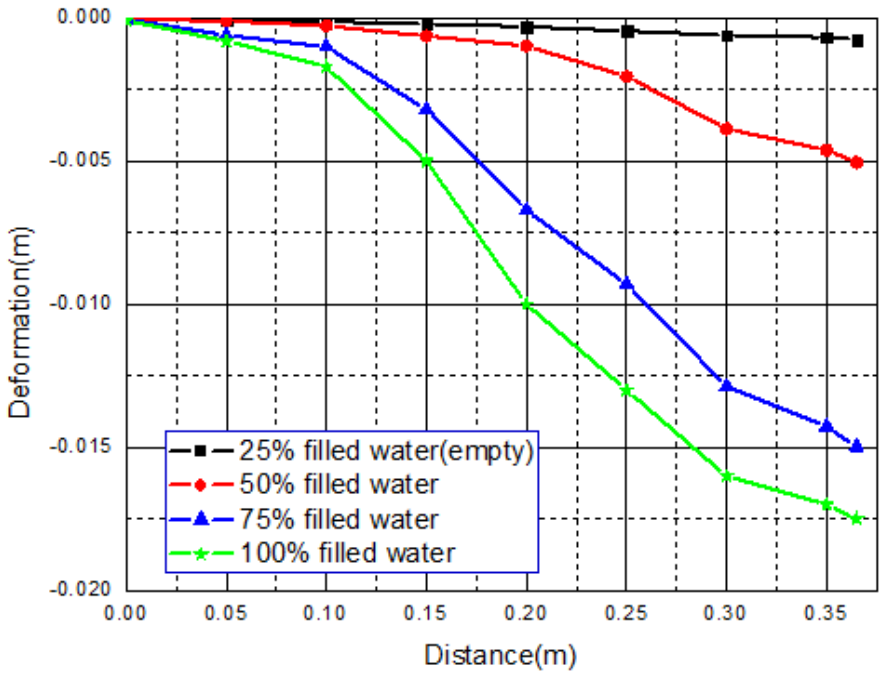

(a) Entry wall

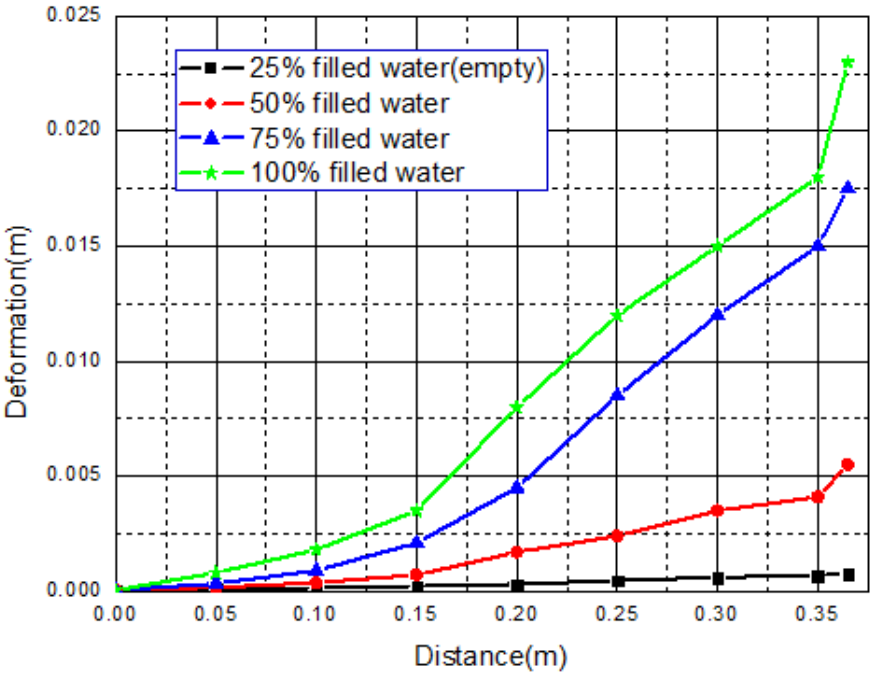

(b) Exit wall

Figure 9. Comparison of entry and exit wall deformations for different water levels

the 75% water level shows the non-symmetric shock wave when the projectile is at the center of the box, the shock pressure at the bottom half is still very close to that when the water level is 100%.

Strains at the exit wall were compared for two different water filling levels, 75% and 100%. Figure 13 shows that the higher water filling level significantly increases the strain at the exit wall resulting from the higher water pressure. The strain curves showed that the high strain level is achieved before the arrival time of the projectile at the exit wall. The high pressure shock wave resulted in high strains before the projectile. The strain was computed at the location which is 50 mm away from the center of the exit wall along the horizontal axis.

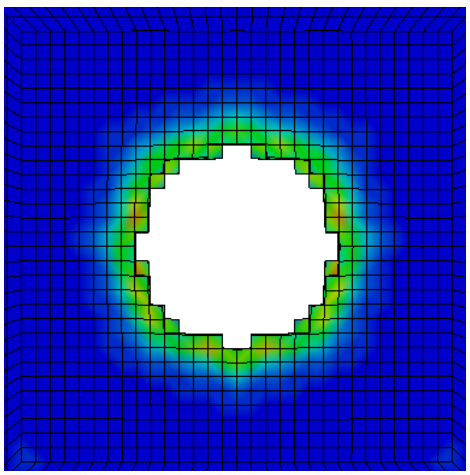

(a) 25% water level

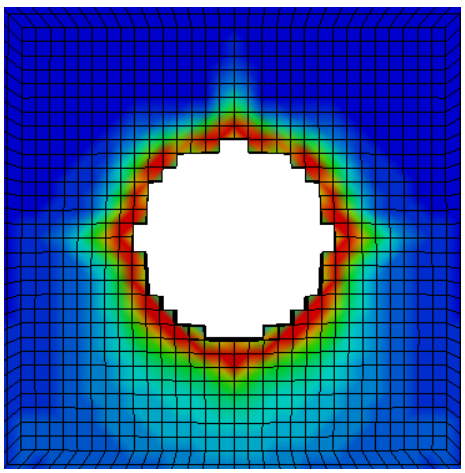

(b) 50% water level

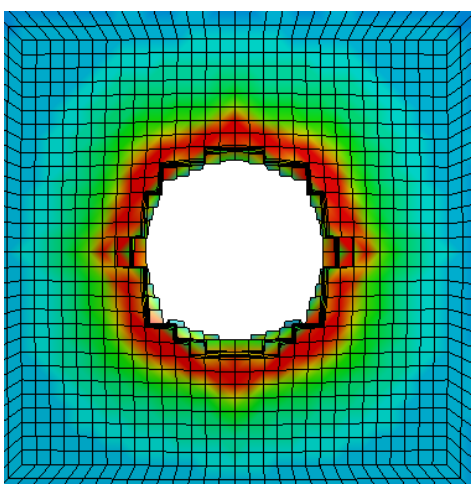

(c) 75% water level

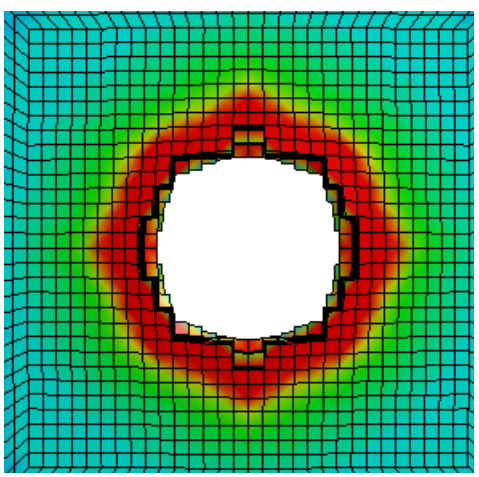

(d) 100% water level

Figure 10. Comparison of residual plastic strains in entry walls for different water levels

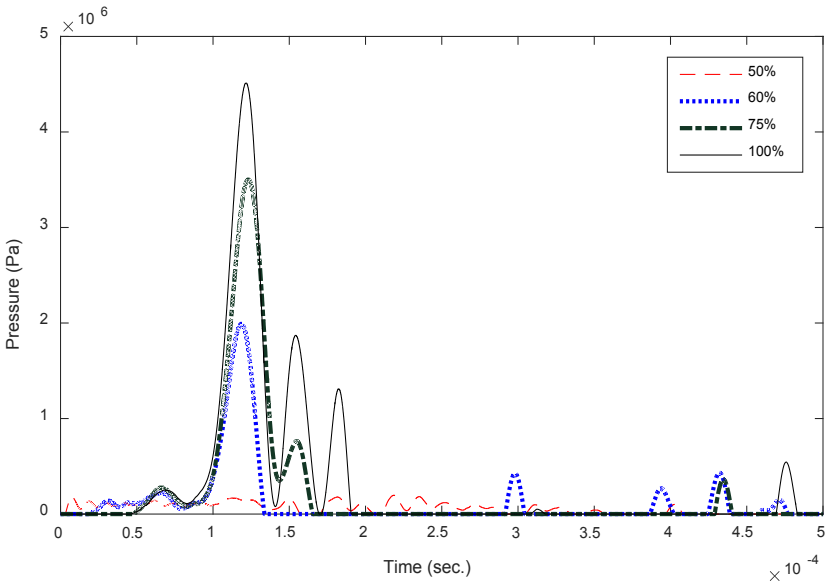

Figure 11. Plot of pressure at sensor location 2 for different water filling levels

3.2. Wall thickness

The projectile nominal velocity is 900 m/s, and the nominal wall thickness of the box is 2.5 mm. It was changed to 1.5 mm and 3.5 mm, respectively. The box is full of water for this study and the subsequent studies unless otherwise mentioned. As expected, the thicker wall results in a greater loss in the projectile velocity as it penetrates through the entry wall. However, once the projectile gets into the box, its velocity varies almost the same rate regardless of the wall thickness. Figure 14 shows the velocity variation as a function of time. The constant velocity at a later time indicates the velocity after coming out of the exit wall. The 3.5 mm thick wall resulted in a larger loss in the velocity during the exit process. For this thick wall, the water pressure was not large enough to make large damage to the exit wall before the projectile arrived at the exit wall. Examining Fig. 14 shows that the additional loss in the projectile speed at the onset of exit wall penetration is 27 m/s for the additional 1.0 mm thickness of the box. In other words, the extra loss in the projectile speed is 27 m/s as the wall thickness increases from 1.5 mm to 2.5 mm, and it is also the same for the wall thickness from 2.5 mm to 3.5 mm.

3.3. Projectile impact velocity

The projectile impact speed was varied such as 300 m/s, 600 m/s, 900 m/s, and 1,200 m/s. The higher impact velocity resulted in shorter time to penetrate the entry wall, which is shown in Fig. 15. The initial steep reduction in the velocity occurred during the penetration process, and the speed reduction is greater for the faster speed than for the slower speed. However, the duration of the steep reduction in velocity is shorter for a faster projectile impact.

Table 5 compares the velocity loss during penetration into either entry or exit wall. The absolute magnitude in the velocity loss is greater for the higher impact speed, but the

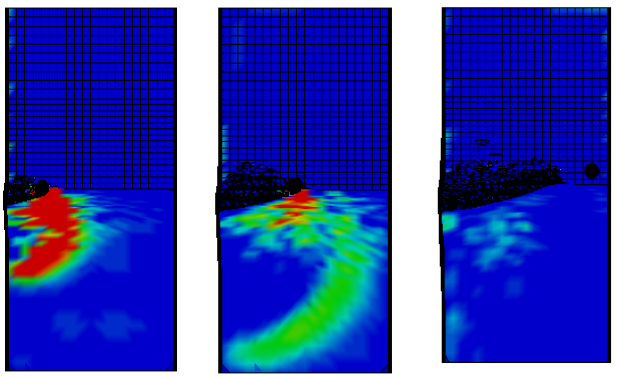

(a) 50% water level

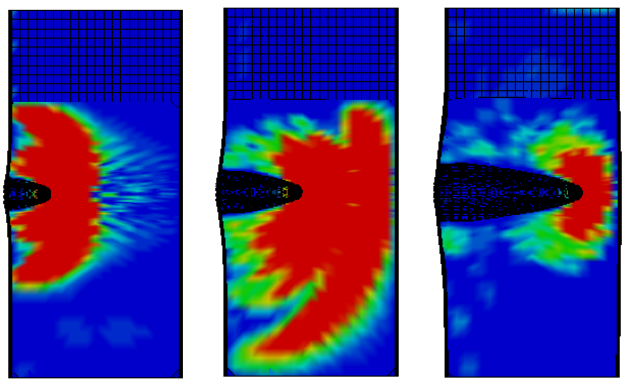

(b) 75% water level

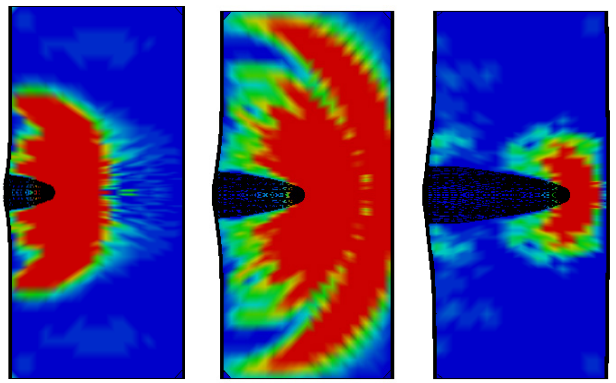

(c) 100% water level

Figure 12. Plot of fluid shock waves for different water levels. (Left, center, and right plots are when the projectile at the quarter, middle, and three quarters length along the box.)

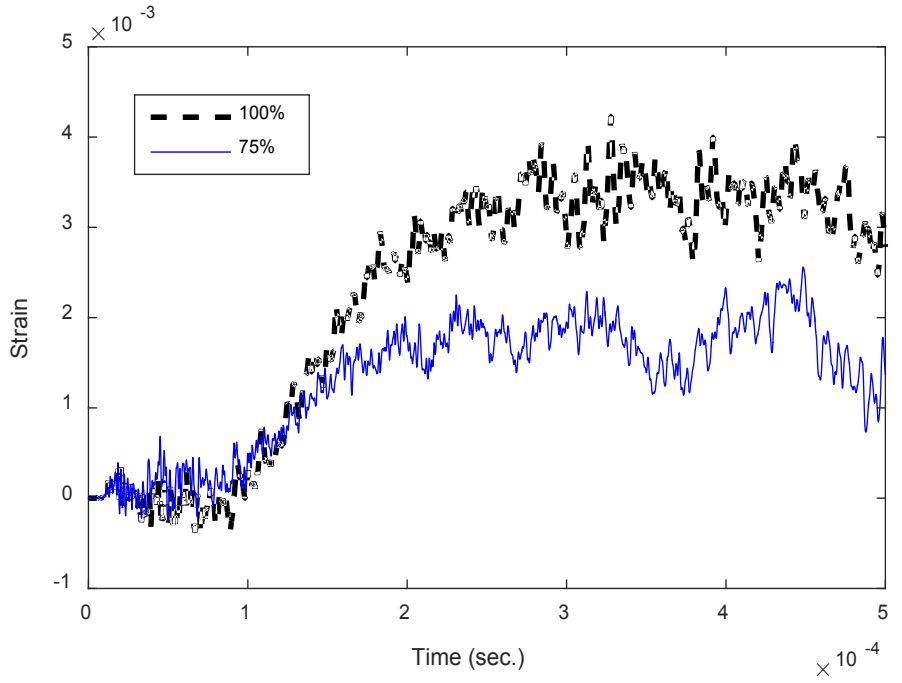

Figure 13. Comparison of strains near the center of the exit wall for different water filling levels.

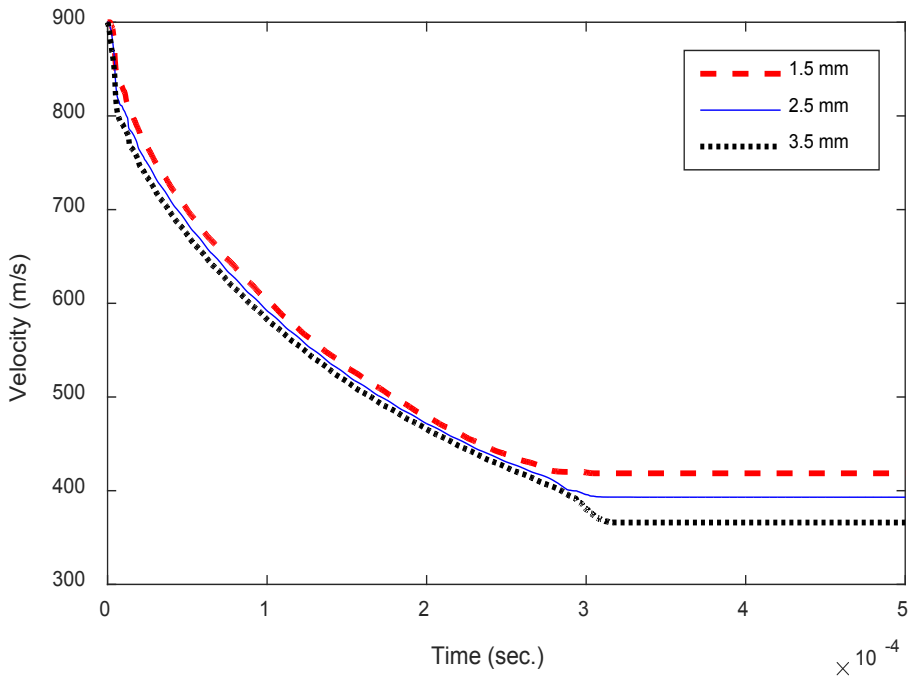

Figure 14. Projectile velocity plot for different wall thickness of box

percentage reduction is smaller for the higher speed. For the exit wall penetration, the fluid pressure with high impact velocity (600 m/s or higher in Table 5) yields severe damage to the exit wall before the projectile reaches the exit wall. As a result, the velocity loss in the projectile is so mall for the exit wall. However, the projectile with the initial impact velocity 300 m/s shows a much greater loss in its speed because the fluid pressure loading is not large enough to yield any significant damage to the exit wall prior to the projectile impact.

Equation (5) is used to predict the velocity time history in Fig. 15 by assuming a constant drag coefficient. The lines in Fig. 15 are the results from the computational simulations while the symbols are obtained using Eq. (5) with the coefficient of drag 0.6. The comparison shows that a constant drag coefficient is a correct assumption for this problem.

Table 5. Change of Velocity after Wall Penetration

Impact velocity	**After entry wall penetration**	**At arrival of exit wall**	**After exit wall penetration**	**remarks**
300 m/s	252 m/s (16%)	122 m/s	85 m/s (30.3%)	No damage due to fluid pressure on exit wall
600 m/s	508 m/s (16%)	260 m/s	243 m/s (6.5%)	Exit wall damage before projectile arrival at exit wall due to prior fluid pressure loading
900 m/s	773 m/s (14.1%)	414 m/s	393 m/s (5.1%)	
1200 m/s	1043 m/s (13.1%)	561 m/s	539 m/s (4.0%)	

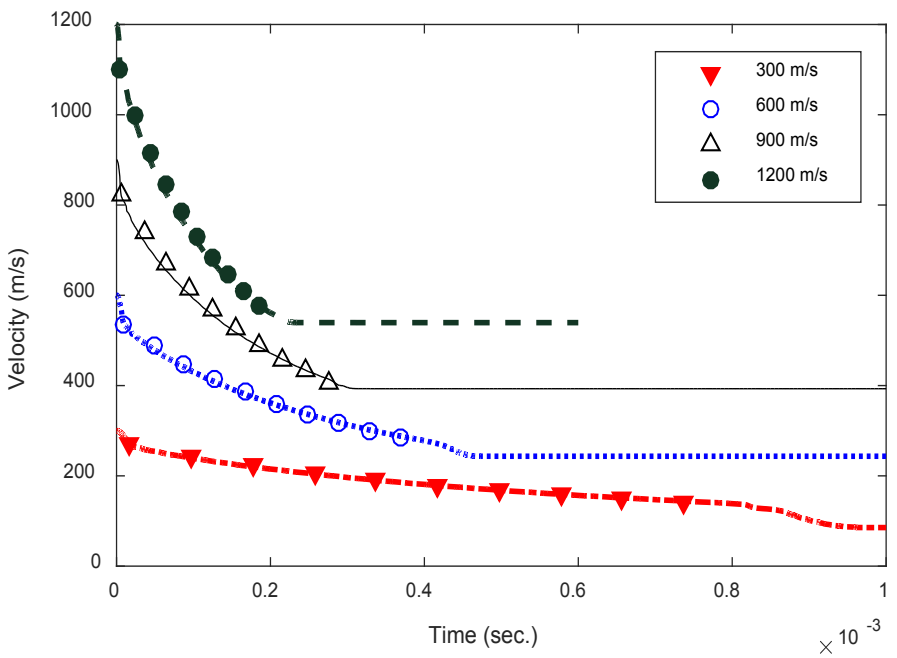

Figure 15. Projectile velocity plot for different initial impact speeds (Lines are the computational results and symbols are from Eq. (5)).

The total loss in the linear moment of the projectile from the initial impact to the final exit out of the box was almost linear to the impact velocity. For the present projectile (8g), the total loss in the linear momentum was fitted closely using the following equation:

$$\Delta(m\mathrm{v})_{loss} = 0.004\mathrm{v}+0.504 \tag{8}$$

where v is the speed in m/s, and the linear momentum has the unit kg-m/s. This equation states that the loss in the linear momentum of the projectile increase about 4 kg-m/s for the increase of the impact speed of 1 m/s. On the other hand, the total loss in the kinetic energy was very well represented by a quadratic function of

$$\Delta\left(KE\right)_{loss} = 0.0063\mathrm{v}^2 + 0.2\mathrm{v}+50 \tag{9}$$

in which the kinetic energy is measured as N-m.

The deformed shapes of the entry and exit walls are plotted in Fig. 16. The entry wall has a smooth deformed shape and it is in the opposite direction to the projectile movement. The magnitude of the deformation is greater for the faster impact speed. However, there is an ultimate deformed shape of the entry wall. As the impact speed increases, the increment in the deformed shape becomes lesser and lesser approaching the maximum shape. On the other hand, the deformed shape at the exit face showed that the opening had steeper deformation with a higher impact velocity as shown in Fig. 16(b). The comparison of Figs. 9 and 16 shows that the change in either the water level or the projectile velocity results in a comparable change in the exit wall deformation.

The resultant residual plastic strains are compared in Fig. 17 for different initial impact velocities. The plots indicate that as the velocity becomes 900 m/s, the exit hole has tearing along the diagonal directions. When the velocity is 1200 m/s, the diagonal tearing is very significant and the plastic strain contours are changed to roughly a square shape.

The fluid shock pressures are plotted in Fig. 18 for different initial impact velocities. The plot for 900 m/s is shown in Fig. 12(c) so that it is omitted in Fig. 18. Because the projectiles have different velocities; the times when the projectiles arrive at the first quarter, middle, and the last quarter length of the box are different. The figure shows that the fluid shock pressure is greater as the projectile reaches the exit wall for the higher impact velocity, which produced larger plastic strain in the wall.

The peak pressure at the sensor location 2 can be fitted very closely using the quadratic function of

$$p_{\max} = 6.7\mathrm{v}^2 - 2000\mathrm{v} + 9x10^5 \tag{10}$$

where p and v are the peak pressure and the impact velocity, respectively. Comparing Eqs. (7) and (10) suggests that the peak pressure can be represented approximately as a quadratic function of either the projectile impact velocity or the water level in the box.

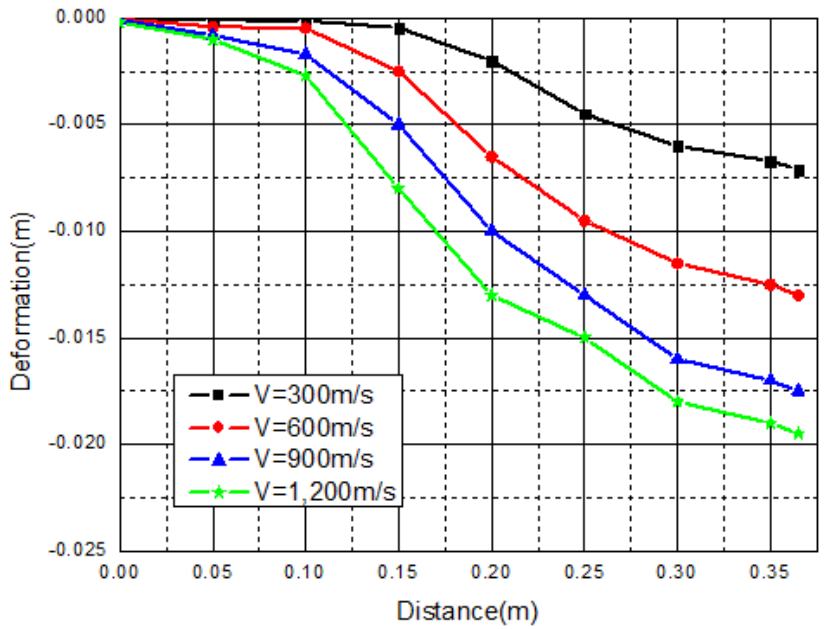

(a) Entry wall

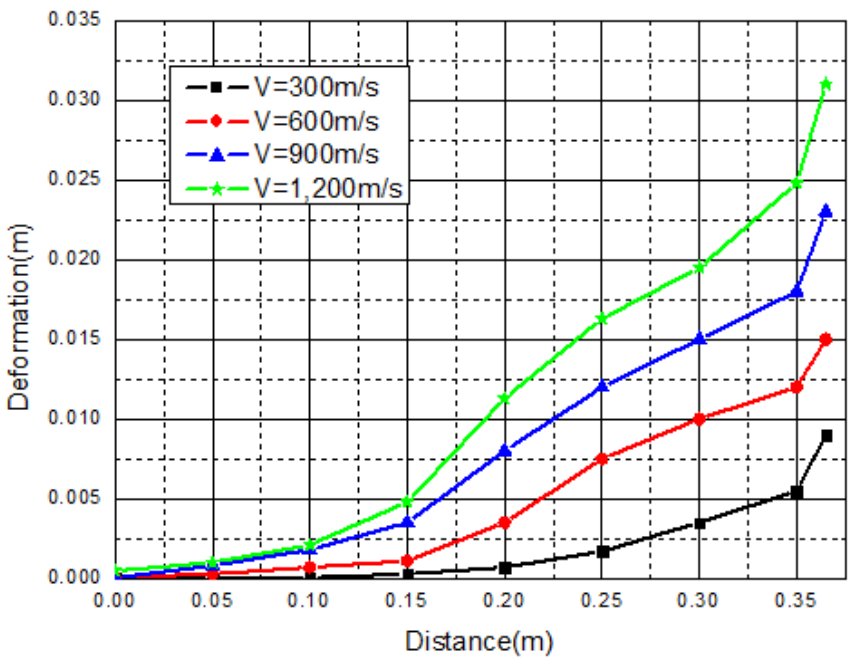

(b) Exit Wall

Figure 16. Plot of deformed shapes of entry and exit walls.

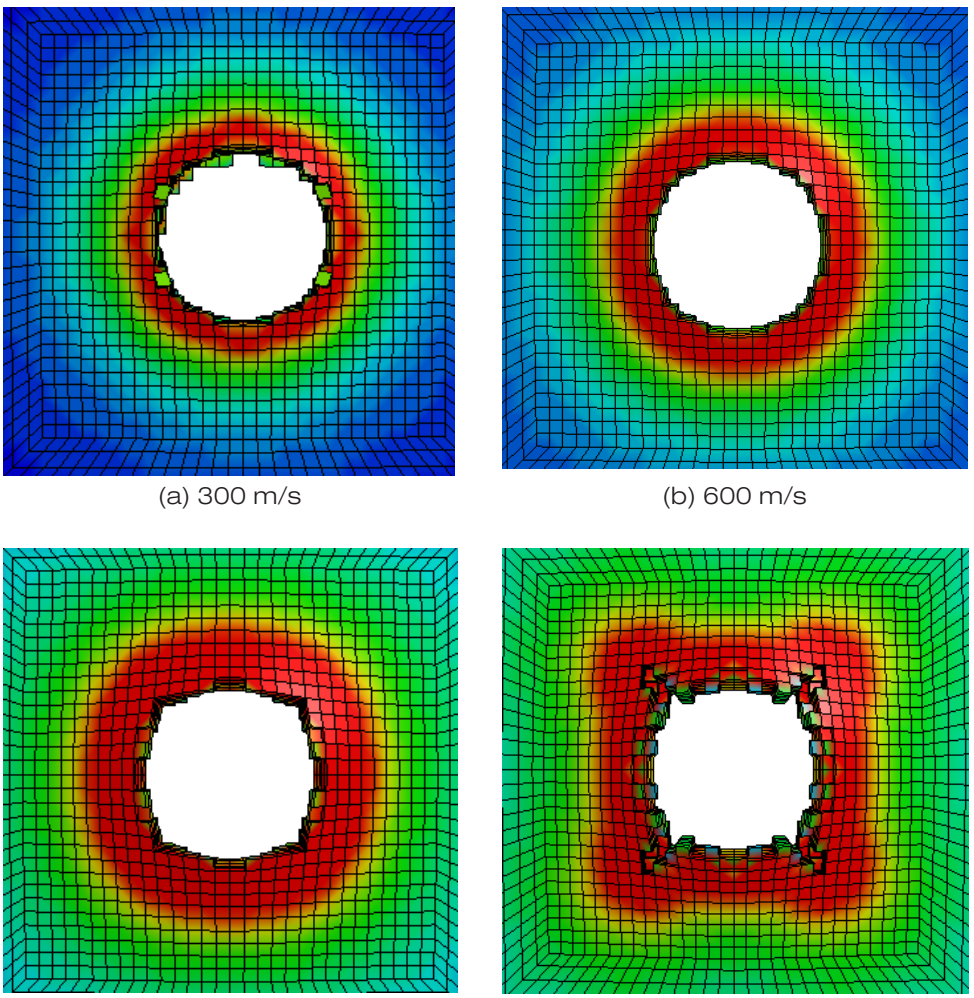

(a) 300 m/s (b) 600 m/s

(c) 900 m/s (d) 1200m/s

Figure 17. Comparison of residual plastic strains in exit walls for different initial impact velocities

3.4. Projectile mass

The projectile mass was varied. The original mass was 8g, and it was changed to 4g and 16g, respectively. When the mass became heavier, it took much shorter time to penetrate the impact wall. As a result, the velocity just after the entry wall penetration is higher for the greater mass so that it takes less time for the heavier projectile to pass through the box as seen in Fig. 19. The total loss in the linear momentum as well as kinetic energy was examined for the different projectile mass. Then, the effect of the mass change was included in Eqs. (8) and (9) as follows

$$\Delta(m\mathrm{v})_{loss} = \left(0.004\mathrm{v}+0.504\right)\left[1+0.4\left(\frac{m-m_o}{m_o}\right)m_o - 0.2\left(\frac{m-m_o}{m_o}\right)^2\right] \tag{11}$$

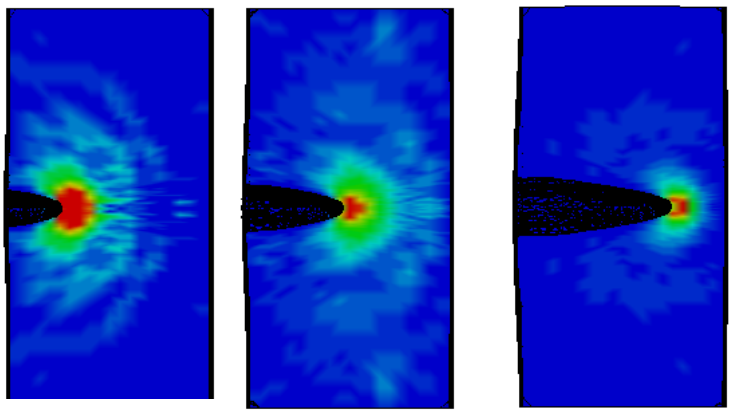

(a) 300 m/s

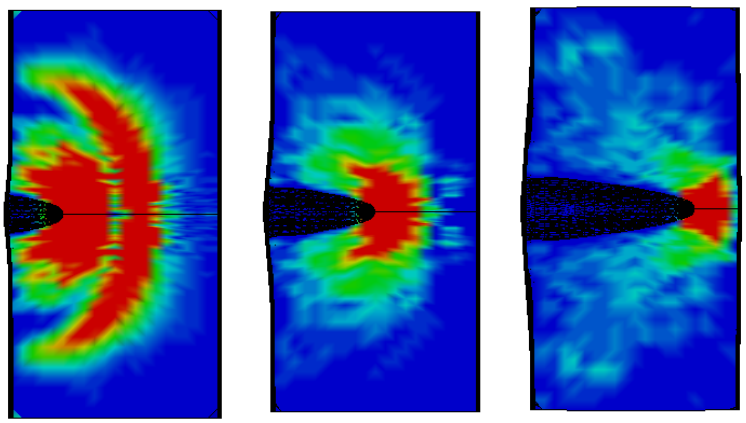

(b) 600 m/s

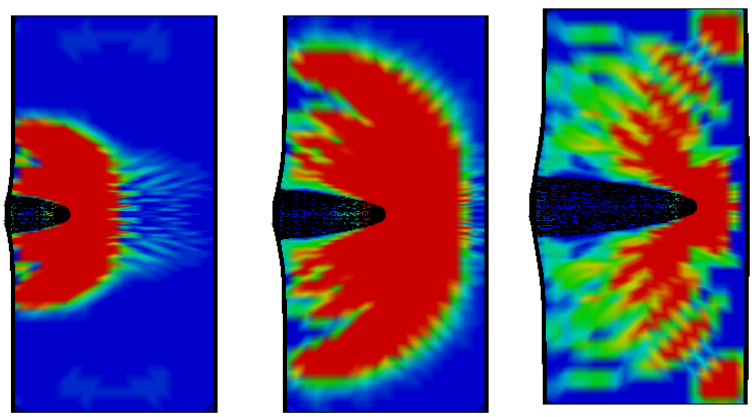

(c) 1200 m/s

Figure 18. Plot of fluid shock wave propagation for different impact velocities (Left, center, and right plots are when the projectile at the quarter, middle, and three quarters length along the box.)

$$\Delta(KE)_{loss} = \left(0.0063\mathrm{v}^2 + 0.2\mathrm{v}+50\right)\left[1+0.66\left(\frac{m-m_o}{m_o}\right)m_o - 0.26\left(\frac{m-m_o}{m_o}\right)^2\right] \tag{12}$$

where m is the projectile mass, and m_o is the reference mass which is 8g for the above equations. Furthermore, if the wall thickness effect is included, the total loss in the linear momentum and kinetic energy may be expressed as

$$\Delta(m\mathrm{v})_{loss} = \left(0.004\mathrm{v}+0.504\right)\left[1+0.4\left(\frac{m-m_o}{m_o}\right)m_o - 0.2\left(\frac{m-m_o}{m_o}\right)^2\right]\left[1+0.13\left(\frac{h-h_0}{h_o}\right)\right] \tag{13}$$

$$\Delta(KE)_{loss} = \left(0.0063\mathrm{v}^2 + 0.2\mathrm{v}+50\right)\left[1+0.66\left(\frac{m-m_o}{m_o}\right)m_o - 0.26\left(\frac{m-m_o}{m_o}\right)^2\right]\left[1+0.08\left(\frac{h-h_o}{h_o}\right)\right] \tag{14}$$

where h is the wall thickness in terms of mm, and h_o is the reference thickness of 2.5 mm. Tables 6 and 7 compare the numerical data to the predicted results using Eqs. (13) and (14). They agree well.

Table 6. Comparison of numerical and predicted loss of linear momentum

Impact velocity (m/s)	Projectile mass (Kg)	Wall thickness (mm)	Numerical loss in linear momentum (Kg-m/s)	Predicted loss in linear momentum (Kg-m/s)	% error
300	0.008	2.5	1.72	1.70	-1.2%
600	0.008	2.5	2.86	2.90	1.4%
900	0.008	2.5	4.03	4.10	1.7%
1200	0.008	2.5	5.29	5.30	0.2%
900	0.004	2.5	3.02	3.08	2.0%
900	0.016	2.5	4.90	4.92	0.4%
900	0.008	3.5	4.25	4.24	-0.2%
900	0.008	1.5	3.82	3.82	0.0%

Table 7. Comparison of numerical and predicted loss of kinetic energy

Impact velocity (m/s)	Projectile mass (Kg)	Wall thickness (mm)	Numerical loss in kinetic energy (N-m)	Predicted loss in linear momentum (Kg-m/s)	% error
300	0.008	2.5	662	617	-6.8%
600	0.008	2.5	2,410	2,320	-3.7%
900	0.008	2.5	5,230	5,150	-1.5%
1200	0.008	2.5	9,200	9,120	0.1%
900	0.004	2.5	3,160	3120	-1.3%
900	0.016	2.5	7,310	7220	-1.2%
900	0.008	3.5	5400	5400	0.0%
900	0.008	1.5	5050	5060	0.2%

The strains at the entry wall were compared for different masses. The strain was calculated at the location which is 50 mm away from the center of the entry wall along the horizontal axis. The strain increases as the mass increased, as expected. The increment in the kind-of plateau strains for the change of the projectile mass from 4g to 8g is about the same as that for the change of the projectile mass from 8g to 16g. The pressure in water is not much different for different masses even though there is a measurable difference in their velocities inside water.

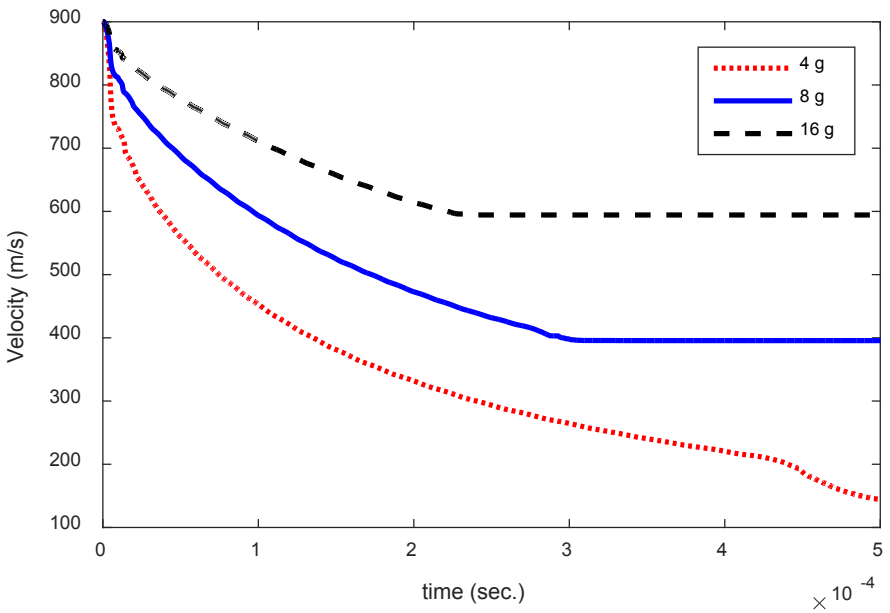

Figure 19. Time history of projectile velocity for different projectile masses

3.5 Impact angle

The impact angle was varied to the water tank as sketched in Fig. 20. The original model had the impact angle $\theta = 0^o$ and it was changed to 30^o and 45^o, respectively. The projectile velocity is plotted in Fig. 21 for different impact angles while the water tank was filled partially or fully. The impact location was still at the center of the impact face. When the water level was 40%, the projectile just after penetration did not contact with water because the water level was low. As a result, the projectile velocity did not decrease for a short while until it plunged into the water inside the box. When the impact location was dry (i.e., water level of 40%), the reduction in the projectile velocity during the penetration process was smaller as compared to other cases with greater water fills. The kinetic energy consumption during penetration was also greater for the higher impact angle. Furthermore, the travel distance through water is longer for the higher angle impact so that the projectile could not penetrate the back face as shown in Fig. 21(b). The projectile velocity became zero after stopped by the exit face.

Figure 22 compares the projectile paths for the two different impact angles. The vertical distance measured in the normal direction to the extended impact line was plotted in the figure.

The deviation is greater when the box has less water for the 30° impact. However, for the 45° impact, the projectile inside the tank with a low water level shows initial deviation from the impact line followed by a later return toward the impact line as seen in Fig. 22(b).

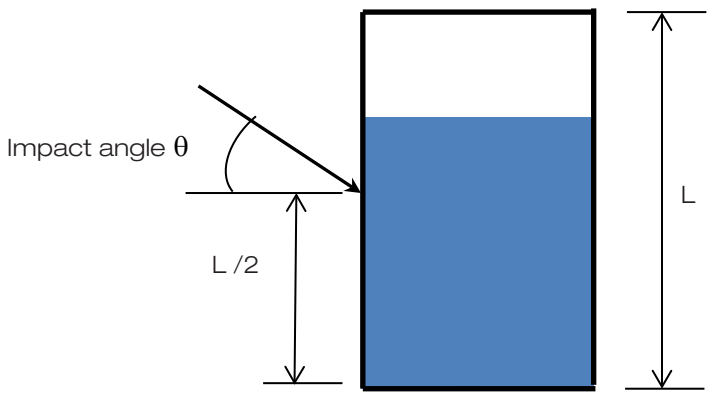

Figure 20. Sketch showing impact angle

3.6 Projectile shape

The projectile shape is sketched in Fig. 23. In this parametric study, all dimensions were fixed as shown in the figure except for the length L which was varied such that the length to the diameter ratio L/D becomes 3, 4.5, and 6, respectively. Two sub-cases were considered. The first sub-case is all three projectiles have the same mass. In other words, the density of each projectile is different such that the mass becomes 8g as before even though the shapes are not spherical. The second sub-case has the constant density. In this subcase, the projectiles of L/D = 3, 4.5, and 6 have the masses of 8g, 11g, and 16g, respectively.

As the projectiles had the same mass, the bullet shape projectiles had a smaller coefficient of drag than the spherical projectile because the diameter of the bullet shape is smaller than the spherical shape. As a result, the reduction in speed was much less for the bullet shape projectile. However, the coefficient of drag was the same for different ratios of L/D. When the density was constant, the longer projectile with the heavier mass has a smaller loss in speed. Hence, this sub-case is similar to the parametric study with the mass change as shown in Fig. 18. However, comparison of Figs. 19 and 24 shows a couple of different responses. First of all, the bullet shape projectile did not show any notable velocity drop during the entry wall penetration. This is because the bullet shape projectile is more effective for penetration. Secondly, the arrival time of the projectile to the exit wall is very close among three different lengths of the bullet shape projectile while the arrival time is very different for the three spherical projectiles.

Comparing the plastic strain at the entry and exit walls, the longer projectile produced larger plastic strain than the shorter projectile as shown in Fig. 25 when both projectiles had the same mass. When the projectile was longer and heavier, it certainly produced much

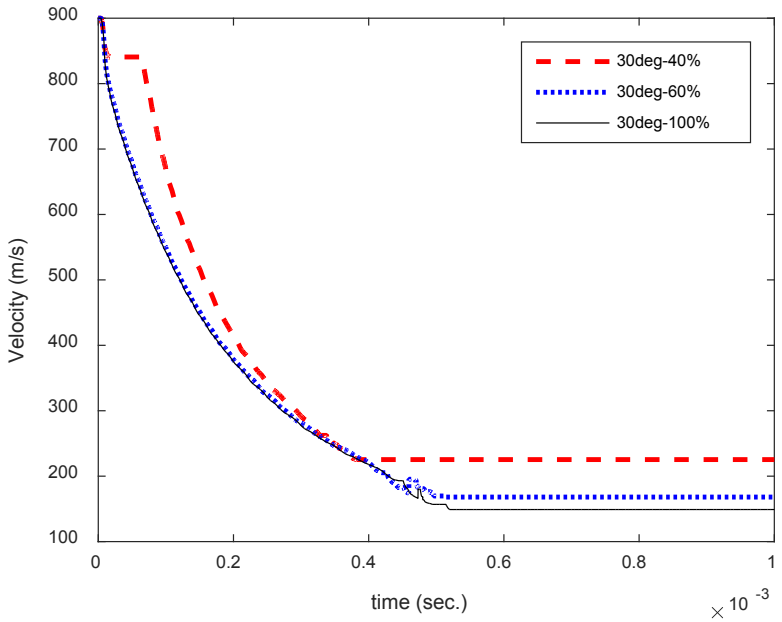

(a) 30° impact

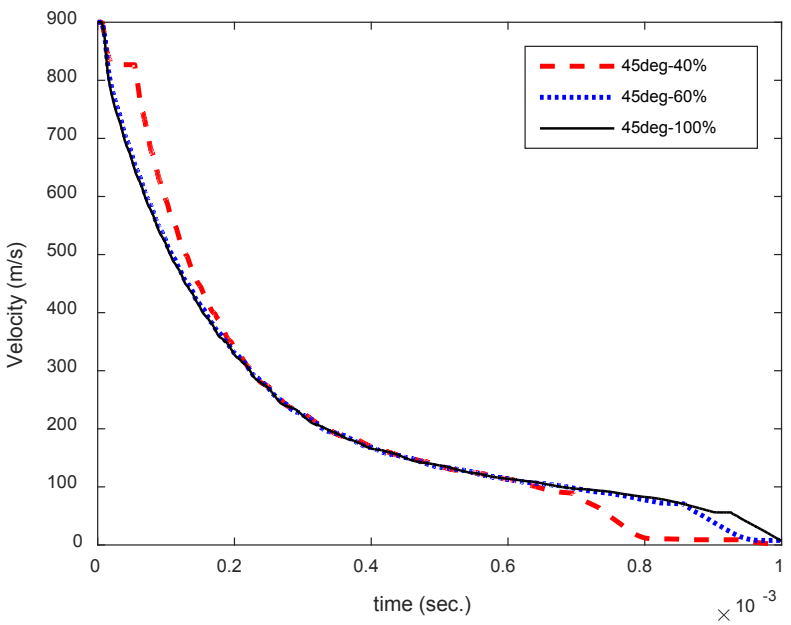

(b) 45° impact

Figure 21. Plot of projectile velocity time history for different impact angles to partially or fully filled water tank

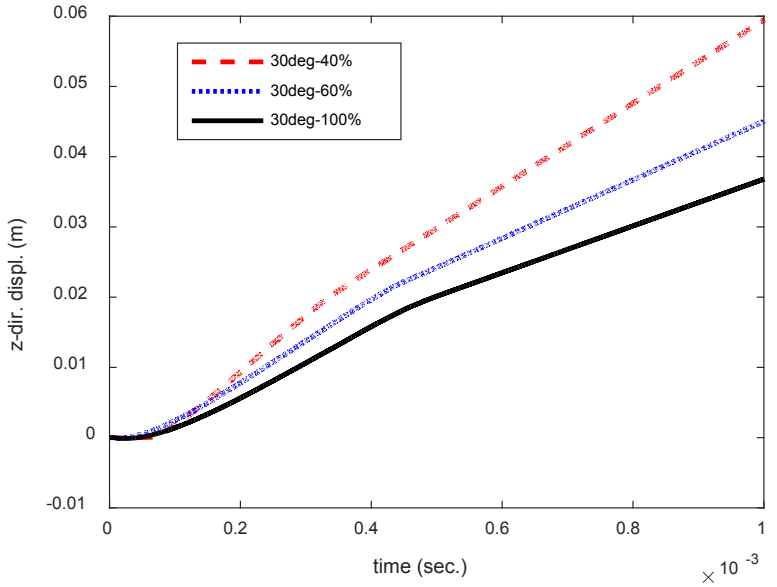

(a) 30° impact

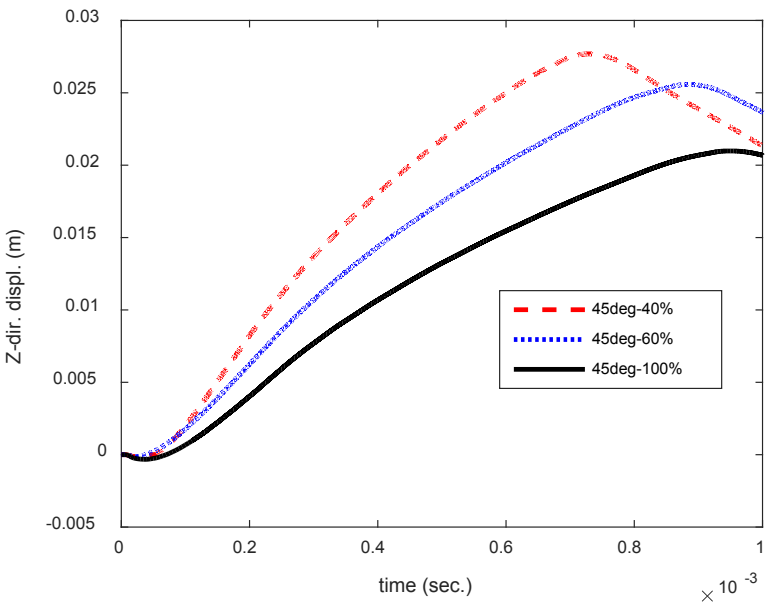

(b) 45° impact

Figure 22. Plot of projectile path deviation time history for different impact angles to partially or fully filled box

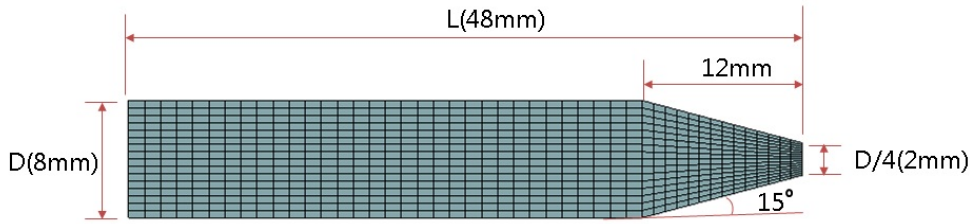

Figure 23. Projectile geometry

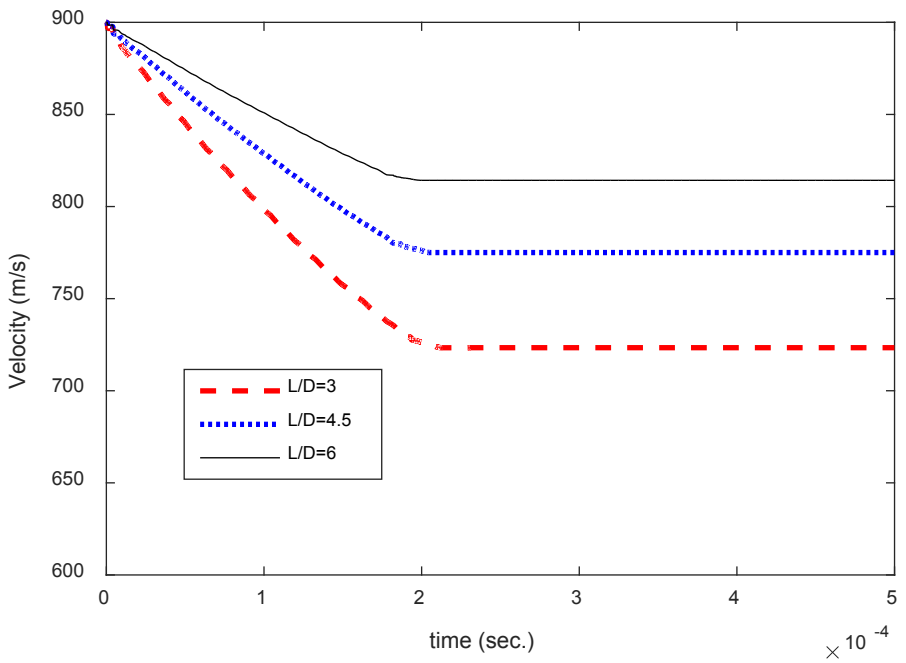

Figure 24. Comparison of projectile velocities for different projectile lengths with different masses.(i.e., constant mass density)

greater plastic strains in both the entry and exit walls. On the other hand, the spherical shape projectile resulted in much larger plastic deformation than the bullet shape projectile even though they had the same mass. Therefore, the spherical shape projectile lost more speed during the penetration process.

However, the bullet shape projectile is prone to deviation from its trajectory. Figure 26 compares the deviations from their line of impact. The figure suggests that such a trajectory deviation is influenced by both the projectile length and mass. Generally, a shorter and lighter projectile had a larger deviation. The projectile with L/D=6 had a negligible deviation. On the other hand, the projectile with L/D=4.5 showed the deviation in either the positive or negative direction depending on its mass. When it weighed 11g, it moved to the negative direction while it travelled to the positive direction when it was 8g. The effect of the projectile length

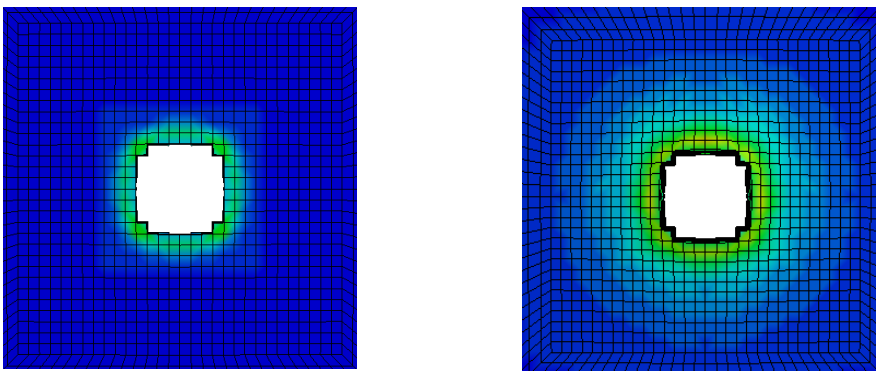

Entry Wall Exit Wall

(a) L/D = 3

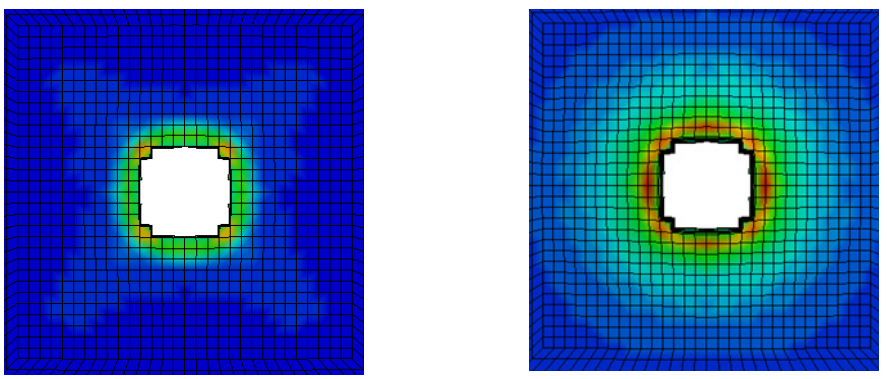

Entry Wall Exit Wall

(b) L/D=6

Figure 25. Comparison of residual plastic strains at entry and exit walls for two different bullet shape projectiles with the same mass

on the trajectory deviation can be explained by examining the fluid pressure around the projectiles. Figure 27 shows the fluid pressure around the three bullet shape projectiles. The surface area in contact with the high fluid pressure is approximately the same for all projectiles. As a result, the shorter projectile is subjected to high pressure to most or all its surface area while the longer projectile has its partial surface area subjected to high pressure. Therefore, the shorter projectile is more prone to deviation from its intended trajectory.

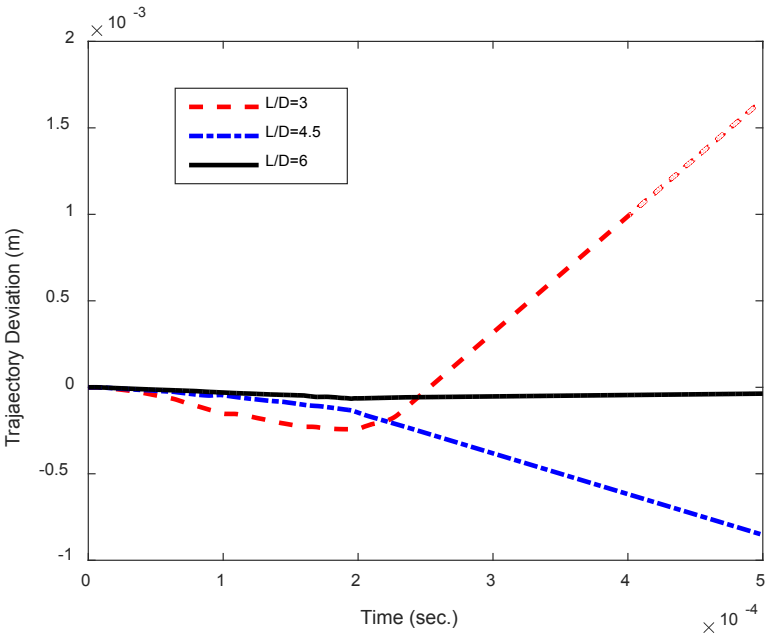

(a) Constant density

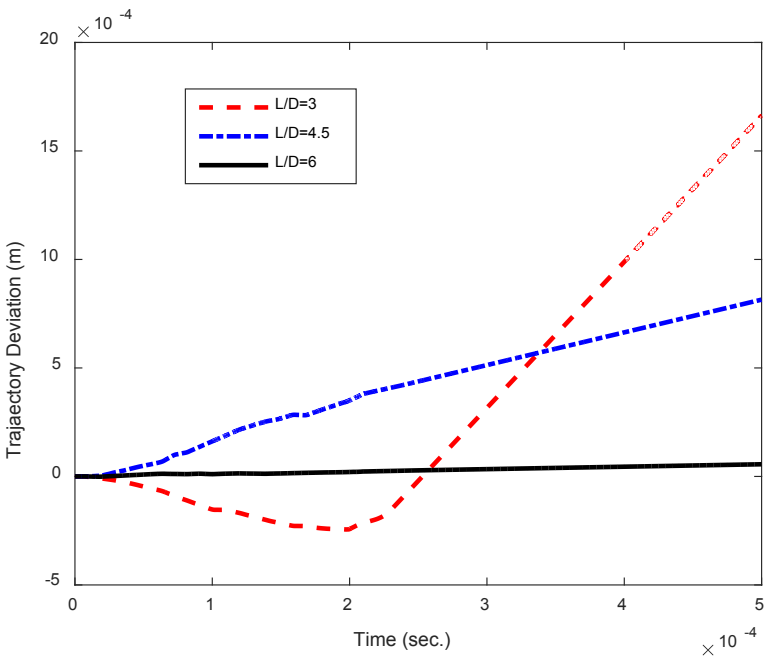

(b) Constant mass

Figure 26. Plot of trajectory deviations of the bullet shape projectiles

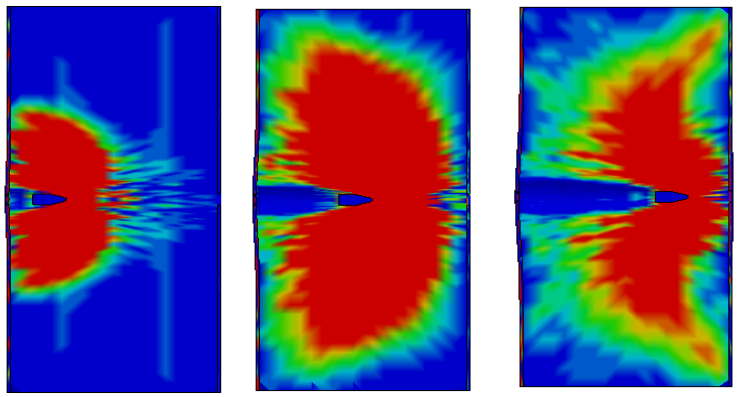

(a) L/D = 3

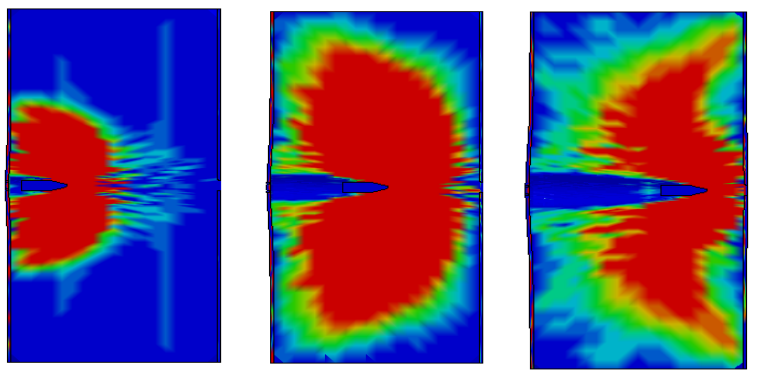

(b) L/D = 4.5

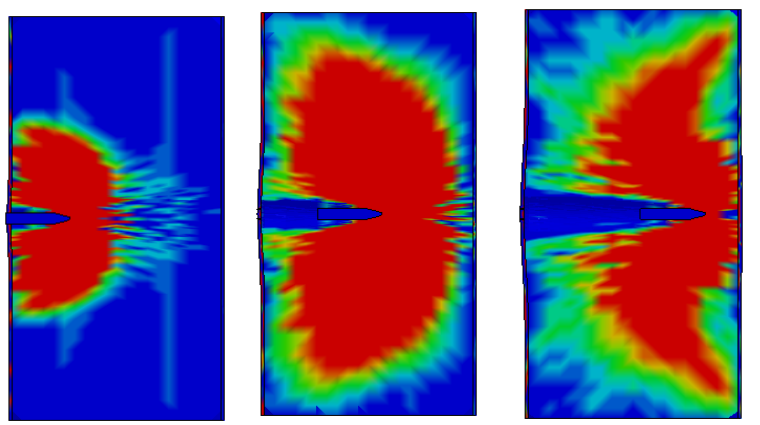

(c) L/D = 6

Figure 27. Fluid pressure around different lengths of projectiles. (Left, center, and right plots are when the projectile at the quarter, middle, and three quarters length along the box.)

4. CONCLUSIONS

A series of parametric study was conducted for a HRAM event using a model which had an aluminum box filled with water and subjected to projectile penetration. The study was undertaken using a numerical technique which coupled the Lagrangian and Eulerian formulations. A base model was analyzed and validated against the experimental data. Then, each parameter was varied one by one individually. Those parameters were the water filling level, wall thickness of structure, projectile impact velocity, projectile mass, impact angle, and projectile shape. The results and discussion are for the specific geometric and material data used in this paper. However, it is expected that they provide some valuable insight to the qualitative characteristics of the HRAM event. Some of the major findings from this specific parametric study are summarized below.

Both the water level inside the box and the projectile velocity influenced the pressure loading in the water, which also affected the penetration and deformation in both the entry and exit walls. The change in either the water level or the projectile velocity resulted in a comparable change in the exit wall deformation. The peak pressure can be represented approximately as a quadratic function of either the projectile impact velocity or the water level in the box.

While the 50% water level yielded larger plastic strain at the bottom side than the top side of the entry wall, all other water levels yielded almost the same plastic deformation at the top and bottom sides. The exit wall had higher plastic strains than the entry wall consistently regardless of water level, impact velocity, projectile mass and shape. This suggests that even though the impact velocity is much greater on the entry wall than the exit wall, the fluid shock pressure produces greater plastic deformation in the exit wall. If either the impact speed of the spherical projectile is 900 m/s with the water filling level 60% or the impactor velocity is greater than 500 m/s with full water, fluid shock pressure results in severe plastic deformation to the exit wall before the projectile reaches the wall. Therefore, there is a minimal loss in the projectile velocity as the projectile penetrates the exit wall.

Plastic deformation in both entry and exit walls was more significant for the spherical shape projectile than the bullet shape projectile. Therefore, the latter had a very minor loss in its speed during the penetration process of the entry wall. When the impact speed was 1200 m/s, there were cracks and plastic deformation along the diagonal directions. Therefore, the contours of the plastic strains at the exit wall became a square-like shape for 1200 m/s while those were circular shapes for the lower speeds.

- The total loss in the linear momentum of the projectile during the HRAM process (i.e. from initial impact to final exit out of the box) can be expressed using the equations in the previous section, Eqs. (13) and (14). Those equations stated above were obtained for the geometric and material data used in this study.
- The coefficient of drag force could be assumed constant during the HRAM event. For the spherical projectile, the coefficient was 0.6. The spherical projectile trajectory is deviated from the impact line if either the water level is not full or the initial impact is not normal to the entry wall. For the bullet shape projectiles, the shorter and lighter bullet was more prone to trajectory deviation, as expected. This could be explained by examining the fluid pressure profiles around the projectiles.
- The present findings were obtained for the models studied here. However, they can provide insight to qualitative characteristics of the HRAM event to enhance further understanding of the process.

REFERENCES

[1] Fuhs, A. E., Ball, R. E., and Power, H. L., "FY 73 Hydraulic Ram Studies", NPS-57Fu74021, 1974.

[2] Power, H. L., "FY 74 Experimental Hydraulic Ram Studies", NPS-57Ph74081, 1974.

[3] Ball, R. E., "Prediction of the Response of the Exit Wall of the NWC 50 Cubic Feet Tank to Hydraulic Ram", NPS Report, NPS-57BP74031, 1974.

[4] Ball, R. E., "Aircraft Fuel Tank Vulnerability to Hydraulic Ram: Modification Of The Northrop Finite Element Computer Code Br-1 To Include Fluid- Structure Interaction—Theory and User's Manual for Br-1hr", NPS-57Bp74071, 1974.

[5] Power, H. L., "FY 75 Experimental Hydraulic Ram Studies", NPS-57Ph75061, 1975.

[6] Page, B., "Entry Wall Strain Measurements During Hydraulic Ram", Master's Thesis, NPS,1975.

[7] Patterson, J. W., "Fuel Cell Pressure Loading During Hydraulic Ram", Master's Thesis, NPS, 1975.

[8] Duva, A. N., "Hydraulic Ram Effect on Composite Fuel Entry Walls", Master's Thesis, NPS, 1976.

[9] Ezzard, H. S. Jr., "A Study of the Failure of Joints in Composite Material Fuel Cells due to Hydraulic Ram Loading", Master's Thesis, NPS, 1976.

[10] Kimsey, K. D., 1980, "Numerical Simulation of Hydrodynamic Ram," U.S. Army Ballistic Research Laboratory, Aberdeen Proving Ground, MD, Report No. ARBRL-TR-02217.

[11] parks, C. E., Hinrichsen, R. L., and Friedmann, D., 2005, "Comparison and Validation of Smooth Particle Hydrodynamics (SPH) and Coupled Euler Lagrange (CEL) Techniques for Modeling Hydrodynamic Ram," AIAA Paper No. 2005-2331.

[12] Varas, D., Zaera, R., and Lopez-Puente, J., 2009, "Numerical Modelling of the Hydrodynamic Ram Phenomenon," Int. J. Impact Eng., 36(3), pp. 363–374.

[13] Liang, C., Bifeng, S., and Yang, P., 2011, "Simulation Analysis of Hydrodynamic Ram Phenomenon in Composite Fuel Tank to Fragment Impact," 3rd International Conference on Measuring Technology and Mechatronics Automation (ICMTMA), Shanghai, China, Jan. 6–7, pp. 241–244.

[14] Poehlmann-Martins, F., Gabrys, J., and Souli, M., 2005, "Hydrodynamic Ram Analysis of Non-Exploding Projectile Impacting Water," ASME Paper No. PVP2005-71658.

[15] Vignjevic, R., De, V. T., Campbell, J. C., and Bourne, N. K., 2002, "Modelling of Impact on a Fuel Tank Using Smoothed Particle Hydrodynamics," 5th Conference on Dynamics and Control of Systems and Structures in Space (DCSSS),Kings College, Cambridge, UK, July 18–22.

[16] LS-DYNA keyword user's manual: nonlinear dynamic analysis of structures. Version 971, vols 1 and 2. Livermore Software Technology Corporation; May 2007.

[17] Johnson GR, Cook WH. A constitutive model and data for metals subjected to large strains, high strain rates, and temperatures. In: Proceedings of seventh international symposium, The Hague, The Netherlands; 1983. p. 1–7.